



Helge S. Stein, Siyuan Zhang, Yujiao Li, Christina Scheu*
and Alfred Ludwig*

Photocurrent Recombination Through Surface Segregation in Al–Cr–Fe–O Photocathodes

<https://doi.org/10.1515/zpch-2019-1459>

Received April 27, 2019; accepted June 28, 2019

Abstract: Chemical surface segregation is a design variable in the optimization of photocathodes but has largely been investigated through surface passivation or decoration. In this study a long charge carrier lifetime material, Al–Cr–Fe–O, exhibiting strong photocurrent recombination is investigated for its atomic scale crystallographic and chemical inhomogeneity. Combined scanning transmission electron microscopy and atom probe tomography unveils that insulating Al- and Cr-rich surface layers form during processing. These are discussed to be the primary reason for experimentally observed charge carrier recombination. This study highlights the importance of processing in the design, discovery and optimization of new light absorber materials for photoelectrochemical water splitting.

Keywords: APT; solar water splitting; surface segregation; TEM; thin films.

1 Introduction

In photoelectrochemical (PEC) water splitting efficiency is key [1–4], but complex multicomponent materials render discovery and optimization a challenging task. With new photocathode materials, such as Al–Cr–Fe–O, the primary challenge is to assess materials limitations and judge whether these are intrinsic or not. Two

***Corresponding authors: Christina Scheu**, Max-Planck Institut für Eisenforschung, Max-Planck Str. 1, 40237 Düsseldorf, Germany; and RWTH Aachen, Materials Analytics, RWTH Aachen University, Kopernikusstr. 10, 52074 Aachen, Germany, e-mail: c.scheu@mpie.de; and **Alfred Ludwig**, Chair for Materials Discovery and Interfaces, Institute for Materials, Ruhr-Universität Bochum, Universitätsstr. 150, 44801 Bochum, Germany; and ZGH, Ruhr-Universität Bochum, Universitätsstr. 150, 44801 Bochum, Germany, e-mail: alfred.ludwig@rub.de
Helge S. Stein: Chair for Materials Discovery and Interfaces, Institute for Materials, Ruhr-Universität Bochum, Universitätsstr. 150, 44801 Bochum, Germany
Siyuan Zhang: Max-Planck Institut für Eisenforschung, Max-Planck Str. 1, 40237 Düsseldorf, Germany
Yujiao Li: ZGH, Ruhr-Universität Bochum, Universitätsstr. 150, 44801 Bochum, Germany

Open Access. © 2020 Christina Scheu, Alfred Ludwig et al., published by De Gruyter. This work is licensed under the Creative Commons Attribution 4.0 Public License.

emblematic inherent materials properties are for instance the bandgap and charge carrier lifetime. While hundreds of studies claim to have altered the bandgap of TiO_2 no credible study reduced it towards useable 0.6–1.2 eV (bottom absorber) or 1.5–2.3 eV (top absorber). A similar observation could be made with Fe_2O_3 that despite having an excellent bandgap, lacks the electronic transport properties like charge carrier lifetime and mobility to become a highly efficient photoanode material [2, 5–7].

It is therefore imperative to discover materials with virtually absent inherent limitations in a “fail fast” manner. By high-throughput screening such a candidate system, Al–Cr–Fe–O [8], was identified in a combinatorial materials science outreach program [6, 8]. Photocathodes in this system exhibit a photocurrent onset potential of about 1 V vs. RHE and composition-dependent bandgaps in the range of 1.5 eV and 2.0–2.3 eV [9]. A major shortcoming of Al–Cr–Fe–O photocathodes is however the strong charge carrier recombination observed during chopped light illumination that yields a steady state photocurrent density of only 10–50% of the initial current density (depending on applied potential and without a sacrificial reagent or catalyst) [9]. Charge carrier dynamics measurements found charge carrier lifetimes >500 ps, which suggests that charge carrier recombination should predominantly occur at the semiconductor electrolyte interface. Despite low charge carrier mobilities, incident photon-to-current efficiencies of up to 30% were reported for nanostructured Al–Cr–Fe–O [10, 11]. A detailed atomic resolution study of the surface and near surface chemistry might therefore reveal the reason why this otherwise promising material lacks in performance. The formation of Cr- and Al-rich oxide scales was reported on a number of Al/Cr/Fe containing stainless steels, motivating a combined scanning transmission electron microscopy (STEM) and atom probe tomography (APT) investigation of the elemental distribution along the cross-section of sputtered and post-annealed Al–Cr–Fe–O photocathodes [12–14]. The findings of this study highlight the importance of chemical surface segregation as a pertinent design variable to be considered for solar water splitting metal oxides.

2 Results

2.1 Analytical STEM

To investigate the morphology, crystal and electronic structure along the growth direction, i.e. the inverse direct light absorption path, analytical STEM is utilized. The overview STEM high-angle annular dark field (HAADF) images in Figure 1a–c show three regions of interest along the depth of the material. From

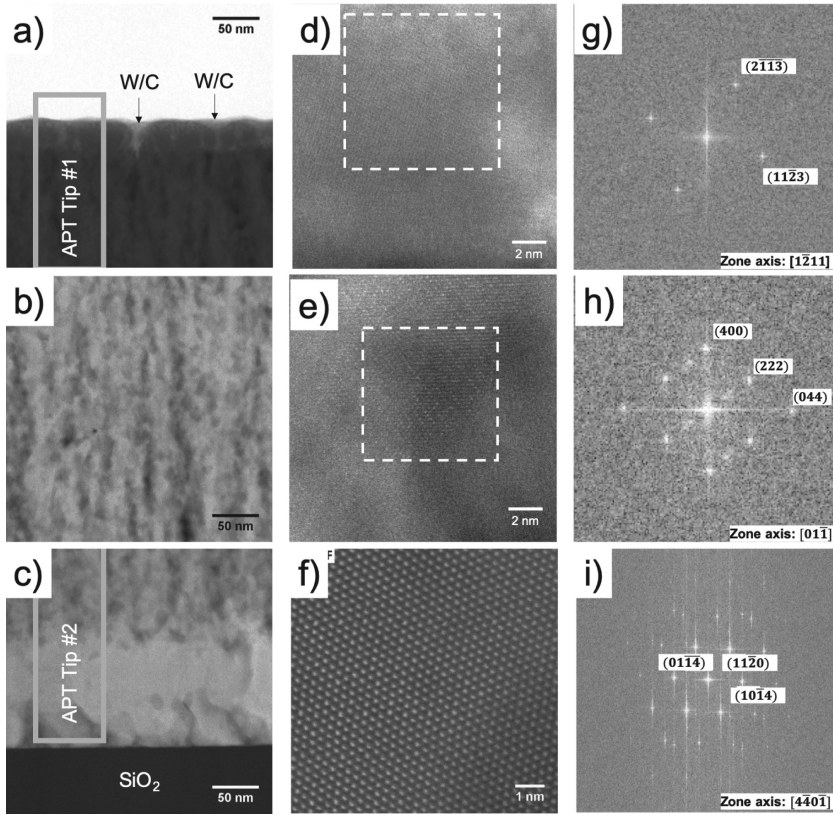


Fig. 1: Results of analytical STEM: High resolution STEM HAADF images of the top, middle, and bottom regions are shown at different magnifications in (a–c and d–f) with their respective fast Fourier transform (FFT) in (g–i), where selected crystallographic planes are indexed. Arrows in (a) indicate W/C from FIB processing. The boxes in (d) and (e) indicate the region where selective region FFT was performed. The top material (a, d, (g) is identified to be of a corundum structure (α - A_2O_3), the middle material (b, (e), (h) is identified to be of a cubic α -(A,B,C) $_2O_3$ spinel type structure. The bottom material shown in (c), (f), (i) has a corundum structure. Grey insets in (a) and (c) denote regions where APT tips were fabricated.

the substrate interface with SiO_2 to the surface of the film (protected by a W/C layer deposited using focused ion beam (FIB)), these are referred to as the bottom layer (~ 120 nm), the middle layer (~ 600 nm), and the top layer (~ 50 nm). Figure 1c, f, and i show that the bottom layer exhibits comparatively large grains of a corundum type structure with grain sizes ranging from 20 nm to 200 nm. These findings already suggest a morphological inhomogeneity that has previously not been observed by thin film XRD or surface SEM [6, 8].

Al, Cr, and Fe have a +3 oxidation state in their corundum oxides, and the bottom layer is used as an internal standard for the oxidation state analysis by electron energy loss spectroscopy (EELS) due to its excellent crystallinity as shown in Figure 1f [15, 16]. The middle layer (Figure 1b) is nanocrystalline with columnar morphology, as expected from the structure zone diagram for room temperature deposited metal-oxide thin films [17, 18]. Moreover, a defect-rich spinel-type structure (e.g. α -(A,B,C)₂O₃ that is structurally similar to γ -Fe₂O₃) is determined from high-resolution imaging of the crystallites and the corresponding Fast Fourier Transform (FFT) (Figure 1e, h).

Figure 2 shows that the Cr L₃ edge towards the middle layer does not exhibit a chemical shift with respect to the bottom layer, suggesting the Cr oxidation state in the spinel structure remains +3. Moreover, the width of the Cr L₃ edge remains unchanged across the depth of the film. A shift of ~ 0.3 eV to lower energy is observed for the Fe L₃ edge from the middle layer with respect to the bottom layer so that a mixed oxidation state is assumed for Fe, as an integer oxidation state shift from Fe³⁺ to Fe²⁺ would require a shift of ~ 1.7 eV [15]. A mixed +2 and +3 oxidation state is also supported by the width change towards the middle layer of the Fe L₃ edge. The STEM images of the top region in Figure 1a and d exhibit a 30–50 nm thick layer with a crystalline porous morphology. Crystallites can be indexed by the corundum structure, see Figure 1g. Chemical composition measurements by STEM-EDS of the top layer are limited to the average along the thickness of the studied cross-sectional sample. The finding of a strong oxidation state inhomogeneity with both sharp and broad interfaces or even interphases is to the best of our knowledge unique to Al–Cr–Fe–O. The only other, however intentional, chemical gradient in PEC materials is found in gradient doped BiVO₄ [19]. To further elucidate the local 3D composition towards the surface of the film, atom probe tomography (APT) was used.

2.2 Atom probe tomography

APT tips were fabricated from the regions indicated in Figure 1a and c. From APT and STEM the top layer is identified to be of a porous morphology (see 3D atom maps Figure 3c due to clusters visible in the 3D atom maps and only faint contrast with the background in Figure 1a).

The thin film exhibits higher Al-oxide concentrations at the very top (25 nm depth in Figure 3a) followed by a high Cr-oxide concentration (50 nm depth Figure 3a). The Cr-oxide rich layer contains about 76 at.% Cr (cation-only distribution) and is about 5 nm thick. The average cation composition of the entire thin film is determined as Al₈Cr_{55.5}Fe_{36.5}O_x by energy dispersive X-ray spectroscopy

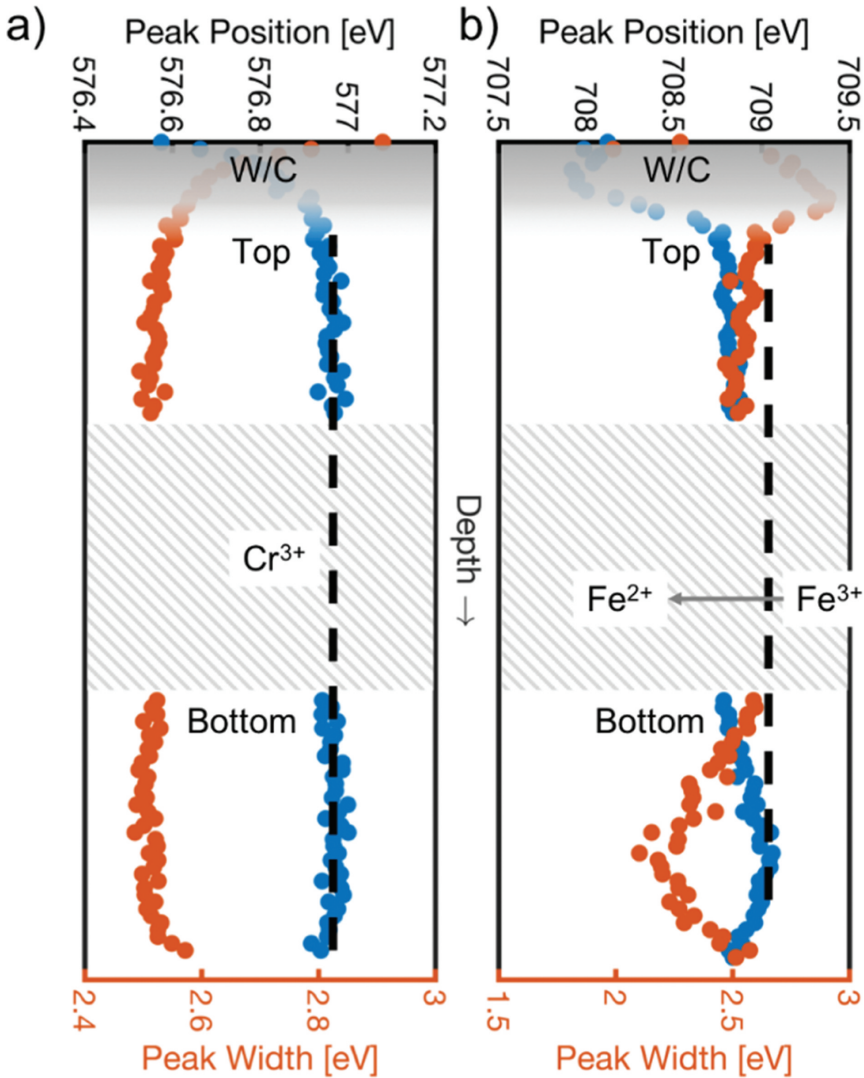


Fig. 2: EELS peak position (blue) and width (orange) of the (a) Cr and (b) Fe L₃ edges. Cr is found to be Cr³⁺ throughout the thin film. At the bottom of the film, Fe is found to be in a Fe³⁺ oxidation state whereas towards the middle and the top it is in a mixed valence state i.e. Fe^{3+/2+}. The grey area at the top of the film indicates the W/C protection layer deposited in the FIB to prevent damage during cutting.

(EDS). At the bottom layer, a Fe-oxide is found by both TEM and APT as shown in Figure 4. The cation composition profiles are plotted in Figure 3b. The cation compositions are observed to be close to where a spinel composition of Cr-Fe-O

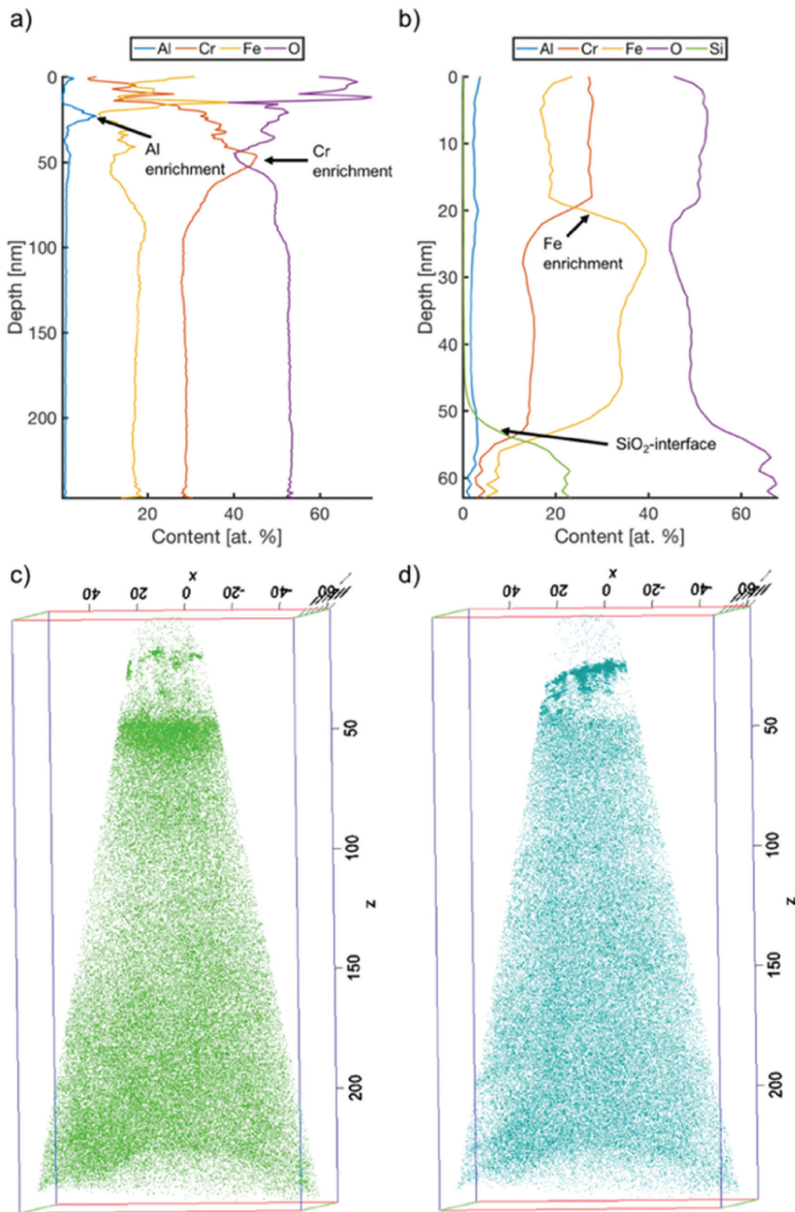


Fig. 3: One dimensional depth profiles (a–b) of atomic concentrations from 3D atom maps (c–d) obtained by APT from (a) the APT tip of the top of the film region in contact with the electrolyte and (b) the APT tip of the bottom film region in contact with the SiO₂ interface. An Al-rich oxide is formed at the top, followed by a Cr-rich oxide. The middle region has a high Cr content and lower Fe and Al content, which is constant over a larger area. Close to the substrate an Fe-rich oxide is formed. Selected 3D atom maps: (c) Cr and (d) AlO, all units in nm.

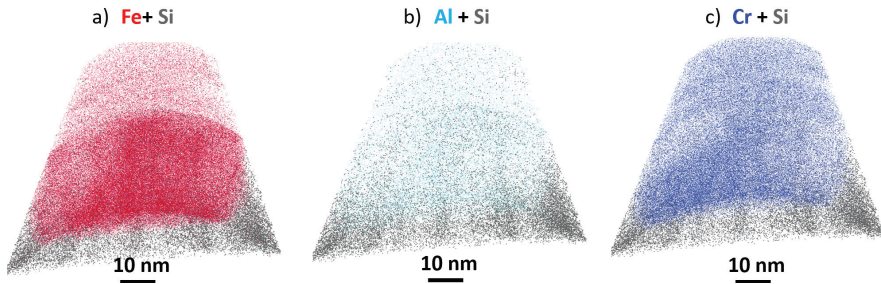


Fig. 4: Selected 3D atom maps of the bottom APT tip. (a) Fe and Si atoms, (b) Al and Si atoms and (c) Cr and Si atoms. Visible is the Al–Cr–Fe–O/Si–O interface as well as the strong Fe enrichment towards greater depth.

would be, i.e. at Cr:Fe ratios of either 2:1 or 1:2 (though the top and bottom material is of corundum type structure), and where highest (absolute) photocurrents were measured [8–10]. The APT results suggest that the interface between the middle and bottom layer appears to be comparably sharp as can be inferred from Figures 1c and 3b as well as 4a–c. The corresponding 3D atom maps are displayed in Figure 4a–c. These suggest that Cr is comparably constantly distributed between the bottom and middle layer whereas Fe exhibits a sharp concentration increase.

3 Discussion

Through combined APT and analytical STEM we discovered that Al–Cr–Fe–O is both morphologically and chemically inhomogeneous along the growth direction which causes a chemical oxidation state shift in Fe through the material. The presented analysis largely confirms previous analyses pertaining crystal structure: the middle region comprising the majority of the p-type material is of a (nanocrystalline and defect rich) cubic spinel type structure [9, 20]. The p-type conductivity is likely caused by antisite defects [7, 21]. It is assumed that some of the excess Fe for a stoichiometric spinel is consumed by the competing phase γ -Fe₂O₃. Under this assumption Al³⁺ should be the main source for p-type doping in Cr-rich Al–Cr–Fe–O [21]. Besides the cubic spinel structure, STEM images reveal the formation of a porous top layer, which is about 30–50 nm thick and of corundum structure. Using APT this layer was identified to be Al- and Cr-rich. Cr₂O₃ and Al₂O₃ are high bandgap and electrically insulating materials, though Cr₂O₃ on the surface (assuming the Al₂O₃ layer is porous enough to allow wetting of the Cr₂O₃) might act as a hydrogen evolution catalyst [11, 22, 23]. The bottom layer is identified to be a Fe-rich corundum structure oxide. As the charge carrier lifetime in p-type Al–Cr–Fe–O is sufficiently long it is suggested that the transients observed

in PEC are from surface recombination [10]. In other surface-limited materials like BiVO_4 surface recombination is associated with a surface defect state that can be passivated through decoration with a catalyst [24]. In Al–Cr–Fe–O however the surface “defect” is an insulating material that prevents charge carrier injection into the electrolyte. With depth, first an Al_2O_3 and then a Cr_2O_3 layer forms. This order can be explained through an Ellingham diagram assessment: Al_2O_3 has a significantly more negative oxide formation enthalpy (higher driving force) than Cr_2O_3 and will therefore be oxidized first. The material was fabricated via reactive magnetron sputtering but might be oxidized further during annealing. Once Al diffuses to the surface and oxidizes it can be assumed to be immobile. The formation of a thin but dense Cr_2O_3 layer might then cut-off further oxygen diffusion to the underlying material as Cr_2O_3 is an oxygen diffusion inhibitor thus dynamically changing the oxidation kinetics during annealing [25, 26]. An improved synthesis route for p-type Al–Cr–Fe–O might therefore be annealing in slightly reducing conditions or heating during deposition.

Concluding, this study confirmed previous crystal structure analyses [8, 9, 11, 20]. However, only the combination of cross-sectional STEM and APT analysis allowed to determine the spatial distribution of the various phases within the depth of the film. Furthermore, the reason for strong charge carrier recombination can be attributed to the formation of a top layer oxide scale of Al_2O_3 and Cr_2O_3 . The finding that the specific processing route chosen leads to a material of interest highlights the necessity to screen both composition and processing spaces simultaneously.

4 Methods

4.1 Reactive magnetron sputter deposition

APT tips and TEM cross-sectional samples were prepared from an Al–Cr–Fe–O materials library (ML) deposited using a previously reported synthesis procedure on a photoresist patterned 100 mm diameter SiO_2/Si wafer [8–10]. The photoresist pattern allowed to divide the ML into measurement areas of 4.5 mm by 4.5 mm. The ML was deposited in a combinatorial reactive magnetron sputter system [27]. Sputtering was performed from elemental targets of high purity at 0.13 Pa at 40 sccm Ar and 2 sccm oxygen flow. Cr and Fe were deposited via DC magnetron sputtering at a power of 150 W. Al was sputtered via radio frequency (RF) sputtering at 100 W. The ML was annealed *ex-situ* in a conventional air furnace at 525 °C for 90 min. The ML was subsequently analysed for composition via EDX using an Oxford INCA X-act detector in a JEOL 5800 scanning electron microscope.

4.2 Preparation of tips and lamella

The measurement area with the overall composition $\text{Fe}_{36.5}\text{Cr}_{55.5}\text{Al}_8\text{O}_x$ was selected for focused ion beam (FIB)-based sample preparation using a standard lift-out as described by Saxey et al [28]. APT tips of p-type Al–Cr–Fe–O were fabricated using FIB as shown in Figure S1. The top APT tip was fabricated in a FEI Nanolab G3CX and the bottom one in a TESCAN Lyra3. TEM cross-sectional samples were fabricated using a standard lift-out technique and subsequent thinning.

4.3 Atom probe tomography (APT)

APT analysis was performed in a LEAPTM 5000 XR (CAMECA Instruments) using the laser mode with an energy of 100 pJ at a pulse frequency of 250 kHz at a detection rate of 0.3% per pulse. Identified species in the mass spectrum were C, Fe, Al, O, OH, C₃, AlO, Cr, C₂, Al₂O, CrO, O₂, O₂H₂, CrO₂, FeO, CrO₃, Fe₂O, Fe₂OH, Cr₂O₅, Cr₂O₅H, H, FeO₂, FeAlO, Fe₂H, Fe₂H₃, Cr₂O₃H₄, and FeAl. Unidentified species account for <0.5% of all atom counts. Reconstruction was performed using the software IVAS 3.6.14. Selected 3D atom maps are shown in Figure S2. Using laser mode oxygen is systematically underestimated by up to 20 at.% [29].

4.4 Scanning transmission electron microscopy (STEM)

STEM analyses were carried out on a FEI Titan Themis microscope operated at 300 kV using an aberration-corrected probe with a convergence semi-angle of 24 mrad and ~ 1 Å probe size. The HAADF detector collects electrons with scattering angles of 73–352 mrad. EELS spectrum imaging was acquired using a Gatan Quantum ERS energy filter in the image-coupled mode to have a 35 mrad collection semiangle. Multivariate statistical analysis was applied to reduce the noise of the spectrum imaging data and extract the position and width of the Cr L₃ and Fe L₃ edges [16].

Acknowledgements: The authors are grateful to the DFG for the financial support within the SPP1613 (LU1175/10-2, DFG SCHE 634/12-2). ZGH is acknowledged for granting access to its facilities.

References

1. M. G. Walter, E. L. Warren, J. R. McKone, S. W. Boettcher, Q. Mi, E. A. Santori, N. S. Lewis, *Chem. Rev.* **110** (2010) 6446.

2. F. E. Osterloh, B. A. Parkinson, *MRS bull.* **36** (2011) 17.
3. B. Parkinson, *Acc. Chem. Res.* **17** (1984) 431.
4. B. Parkinson, *ACS Energy Lett.* **1** (2016) 1057.
5. H. Döschner, J. F. Geisz, T. G. Deutsch, J. A. Turner, *Energy Environ. Sci.* **7** (2014) 2951.
6. M. Woodhouse, B. A. Parkinson, *Chem. Soc. Rev.* **38** (2008) 197.
7. A. Zakutayev, C. M. Caskey, A. N. Fioretti, D. S. Ginley, J. Vidal, V. Stevanovic, E. Tea, S. Lany, *J. Phys. Chem. Lett.* **5** (2014) 1117.
8. J. G. Rowley, T. D. Do, D. A. Cleary, B. A. Parkinson, *ACS Appl. Mater. Interfaces* **6** (2014) 9046.
9. K. Sliozberg, H. S. Stein, C. Khare, B. A. Parkinson, A. Ludwig, W. Schuhmann, *ACS Appl. Mater. Interfaces* **7** (2015) 4883.
10. H. Stein, S. Müller, K. Schwarzburg, D. Friedrich, A. Ludwig, R. Eichberger, *ACS Appl. Mater. Interfaces* **10** (2018) 35869.
11. I. Kondofersky, A. Müller, H. K. Dunn, A. Ivanova, G. Štefanić, M. Ehrensperger, C. Scheu, B. A. Parkinson, D. Fattakhova-Rohlfing, T. Bein, *J. Am. Chem. Soc.* **138** (2016) 1860.
12. A. F. Smith, *Met. Sci.* **9** (2013) 375.
13. Z. G. Zhang, F. Gesmundo, P. Y. Hou, Y. Niu, *Corros. Sci.* **48** (2006) 741.
14. A. U. Seybolt, *J. Electrochem. Soc.* **107**, (1960) 147.
15. P. A. Van Aken, B. Liebscher, *Phys. Chem. Miner.* **29** (2002) 188.
16. S. Zhang, C. Scheu, *Microscopy (Oxf)* **67** (2018) i133.
17. A. Anders, *Thin Solid Films* **518** (2010) 4087.
18. H. Stein, D. Naujoks, D. Grochla, C. Khare, R. Gutkowski, S. Grützke, W. Schuhmann, A. Ludwig, *Phys. Status Solidi A* **212** (2015) 2798.
19. F. F. Abdi, N. Firet, R. van de Krol, *ChemCatChem* **5** (2012) 490.
20. H. S. Stein, S. Jiao, A. Ludwig, *ACS Comb. Sci.* **19** (2017) 1.
21. T. R. Paudel, A. Zakutayev, S. Lany, M. d'Avezac, A. Zunger, *Adv. Funct. Mater.* **21** (2011) 4493.
22. J. A. Crawford, R. W. Vest, *J. Appl. Phys.* **35** (1964) 2413.
23. J. Pappis, W. D. Kingery, *J. Am. Ceram. Soc.* **44** (1961) 459.
24. A. Shinde, D. Guevarra, G. Liu, I. D. Sharp, F. M. Toma, J. M. Gregoire, J. A. Haber, *ACS Appl. Mater. Interfaces* **8** (2016) 23696.
25. W. C. Hagel, *J. Am. Ceram. Soc.* **48** (1965) 70.
26. C. S. Tedmon Jr, *J. Electrochem. Soc.* **113** (1966) 766.
27. A. Ludwig, R. Zarnetta, S. Hamann, A. Savan, S. Thienhaus, *Int. J. Mater. Res.* **99** (2008) 1144.
28. D. W. Saxey, J. M. Cairney, D. McGrouther, T. Honma, S. P. Ringer, *Ultramicroscopy* **107** (2007) 756.
29. A. Devaraj, R. Colby, W. P. Hess, D. E. Perea, S. Thevuthasan, *J. Phys. Chem. Lett.* **4** (2013) 993.

Supplementary Material: The online version of this article offers supplementary material (<https://doi.org/10.1515/zpch-2019-1459>).